EUROPEAN LABORATORY FOR PARTICLE PHYSICS (CERN)

CERN-PPE/97-084
17 July 1997

Searches for Scalar Top and Scalar Bottom Quarks at LEP2

The ALEPH Collaboration

Abstract

Searches for scalar top and bottom quarks have been performed with data collected by the ALEPH detector at LEP. The data sample consists of 21.7 pb^{-1} taken at $\sqrt{s}$ = 161, 170, and 172 GeV and 5.7 pb^{-1} taken at $\sqrt{s}$ = 130 and 136 GeV. No evidence for scalar top quarks or scalar bottom quarks was found in the channels $\tilde{\mathrm{t}} \to \mathrm{c}\chi$, $\tilde{\mathrm{t}} \to \mathrm{b}\ell\tilde{\nu}$, and $\tilde{\mathrm{b}} \to \mathrm{b}\chi$. For the channel $\tilde{\mathrm{t}} \to \mathrm{c}\chi$ a limit of 67 GeV/c^2 has been set on the scalar top quark mass, independent of the mixing angle between the supersymmetric partners of the left and right-handed states of the top quark. This limit assumes a mass difference between the $\tilde{\mathrm{t}}$ and the χ of at least 10 GeV/c^2. For the channel $\tilde{\mathrm{t}} \to \mathrm{b}\ell\tilde{\nu}$ the mixing-angle independent scalar top limit is 70 GeV/c^2, assuming a mass difference between the $\tilde{\mathrm{t}}$ and the $\tilde{\nu}$ of at least 10 GeV/c^2. For the channel $\tilde{\mathrm{b}} \to \mathrm{b}\chi$, a limit of 73 GeV/$c^2$ has been set on the mass of the supersymmetric partner of the left-handed state of the bottom quark. This limit is valid if the mass difference between the $\tilde{\mathrm{b}}$ and the χ is at least 10 GeV/c^2.

(To be submitted to Physics Letters B)

The ALEPH Collaboration

R. Barate, D. Buskulic, D. Decamp, P. Ghez, C. Goy, J.-P. Lees, A. Lucotte, M.-N. Minard, J.-Y. Nief, B. Pietrzyk

Laboratoire de Physique des Particules (LAPP), IN^{2}P^3-CNRS, 74019 Annecy-le-Vieux Cedex, France

M.P. Casado, M. Chmeissani, P. Comas, J.M. Crespo, M. Delfino, E. Fernandez, M. Fernandez-Bosman, Ll. Garrido,[15] A. Juste, M. Martinez, G. Merino, R. Miquel, Ll.M. Mir, C. Padilla, I.C. Park, A. Pascual, J.A. Perlas, I. Riu, F. Sanchez, F. Teubert

Institut de Física d'Altes Energies, Universitat Autònoma de Barcelona, 08193 Bellaterra (Barcelona), Spain[7]

A. Colaleo, D. Creanza, M. de Palma, G. Gelao, G. Iaselli, G. Maggi, M. Maggi, N. Marinelli, S. Nuzzo, A. Ranieri, G. Raso, F. Ruggieri, G. Selvaggi, L. Silvestris, P. Tempesta, A. Tricomi,[3] G. Zito

Dipartimento di Fisica, INFN Sezione di Bari, 70126 Bari, Italy

X. Huang, J. Lin, Q. Ouyang, T. Wang, Y. Xie, R. Xu, S. Xue, J. Zhang, L. Zhang, W. Zhao

Institute of High-Energy Physics, Academia Sinica, Beijing, The People's Republic of China[8]

D. Abbaneo, R. Alemany, A.O. Bazarko,[1] U. Becker, P. Bright-Thomas, M. Cattaneo, F. Cerutti, G. Dissertori, H. Drevermann, R.W. Forty, M. Frank, R. Hagelberg, J.B. Hansen, J. Harvey, P. Janot, B. Jost, E. Kneringer, J. Knobloch, I. Lehraus, P. Mato, A. Minten, L. Moneta, A. Pacheco, J.-F. Pusztaszeri,[20] F. Ranjard, G. Rizzo, L. Rolandi, D. Rousseau, D. Schlatter, M. Schmitt, O. Schneider, W. Tejessy, I.R. Tomalin, H. Wachsmuth, A. Wagner[21]

European Laboratory for Particle Physics (CERN), 1211 Geneva 23, Switzerland

Z. Ajaltouni, A. Barrès, C. Boyer, A. Falvard, C. Ferdi, P. Gay, C . Guicheney, P. Henrard, J. Jousset, B. Michel, S. Monteil, J-C. Montret, D. Pallin, P. Perret, F. Podlyski, J. Proriol, P. Rosnet, J.-M. Rossignol

Laboratoire de Physique Corpusculaire, Université Blaise Pascal, IN^{2}P^3-CNRS, Clermont-Ferrand, 63177 Aubière, France

T. Fearnley, J.D. Hansen, J.R. Hansen, P.H. Hansen, B.S. Nilsson, B. Rensch, A. Wäänänen

Niels Bohr Institute, 2100 Copenhagen, Denmark[9]

G. Daskalakis, A. Kyriakis, C. Markou, E. Simopoulou, A. Vayaki

Nuclear Research Center Demokritos (NRCD), Athens, Greece

A. Blondel, J.C. Brient, F. Machefert, A. Rougé, M. Rumpf, A. Valassi,[6] H. Videau

Laboratoire de Physique Nucléaire et des Hautes Energies, Ecole Polytechnique, IN^{2}P^3-CNRS, 91128 Palaiseau Cedex, France

E. Focardi, G. Parrini, K. Zachariadou

Dipartimento di Fisica, Università di Firenze, INFN Sezione di Firenze, 50125 Firenze, Italy

R. Cavanaugh, M. Corden, C. Georgiopoulos, T. Huehn, D.E. Jaffe

Supercomputer Computations Research Institute, Florida State University, Tallahassee, FL 32306-4052, USA [13,14]

A. Antonelli, G. Bencivenni, G. Bologna,[4] F. Bossi, P. Campana, G. Capon, D. Casper, V. Chiarella, G. Felici, P. Laurelli, G. Mannocchi,[5] F. Murtas, G.P. Murtas, L. Passalacqua, M. Pepe-Altarelli

Laboratori Nazionali dell'INFN (LNF-INFN), 00044 Frascati, Italy

L. Curtis, S.J. Dorris, A.W. Halley, I.G. Knowles, J.G. Lynch, V. O'Shea, C. Raine, J.M. Scarr, K. Smith, P. Teixeira-Dias, A.S. Thompson, E. Thomson, F. Thomson, R.M. Turnbull

Department of Physics and Astronomy, University of Glasgow, Glasgow G12 8QQ,United Kingdom[10]

O. Buchmüller, S. Dhamotharan, C. Geweniger, G. Graefe, P. Hanke, G. Hansper, V. Hepp, E.E. Kluge, A. Putzer, J. Sommer, K. Tittel, S. Werner, M. Wunsch

Institut für Hochenergiephysik, Universität Heidelberg, 69120 Heidelberg, Fed. Rep. of Germany[16]

R. Beuselinck, D.M. Binnie, W. Cameron, P.J. Dornan, M. Girone, S. Goodsir, E.B. Martin, P. Morawitz, A. Moutoussi, J. Nash, J.K. Sedgbeer, P. Spagnolo, A.M. Stacey, M.D. Williams

Department of Physics, Imperial College, London SW7 2BZ, United Kingdom[10]

V.M. Ghete, P. Girtler, D. Kuhn, G. Rudolph

Institut für Experimentalphysik, Universität Innsbruck, 6020 Innsbruck, Austria[18]

A.P. Betteridge, C.K. Bowdery, P. Colrain, G. Crawford, A.J. Finch, F. Foster, G. Hughes, R.W.L. Jones, T. Sloan, E.P. Whelan, M.I. Williams

Department of Physics, University of Lancaster, Lancaster LA1 4YB, United Kingdom[10]

C. Hoffmann, K. Jakobs, K. Kleinknecht, G. Quast, B. Renk, E. Rohne, H.-G. Sander, P. van Gemmeren, C. Zeitnitz

Institut für Physik, Universität Mainz, 55099 Mainz, Fed. Rep. of Germany[16]

J.J. Aubert, C. Benchouk, A. Bonissent, G. Bujosa, J. Carr, P. Coyle, C. Diaconu, A. Ealet, D. Fouchez, N. Konstantinidis, O. Leroy, F. Motsch, P. Payre, M. Talby, A. Sadouki, M. Thulasidas, A. Tilquin, K. Trabelsi

Centre de Physique des Particules, Faculté des Sciences de Luminy, IN^{2}P^3-CNRS, 13288 Marseille, France

M. Aleppo, M. Antonelli, F. Ragusa[12]

Dipartimento di Fisica, Università di Milano e INFN Sezione di Milano, 20133 Milano, Italy.

R. Berlich, W. Blum, V. Büscher, H. Dietl, G. Ganis, C. Gotzhein, H. Kroha, G. Lütjens, G. Lutz, W. Männer, H.-G. Moser, R. Richter, A. Rosado-Schlosser, S. Schael, R. Settles, H. Seywerd, R. St. Denis, H. Stenzel, W. Wiedenmann, G. Wolf

Max-Planck-Institut für Physik, Werner-Heisenberg-Institut, 80805 München, Fed. Rep. of Germany[16]

J. Boucrot, O. Callot,[12] S. Chen, A. Cordier, M. Davier, L. Duflot, J.-F. Grivaz, Ph. Heusse, A. Höcker, A. Jacholkowska, M. Jacquet, D.W. Kim,[2] F. Le Diberder, J. Lefrançois, A.-M. Lutz, I. Nikolic, M.-H. Schune, L. Serin, S. Simion, E. Tournefier, J.-J. Veillet, I. Videau, D. Zerwas

Laboratoire de l'Accélérateur Linéaire, Université de Paris-Sud, IN^{2}P^3-CNRS, 91405 Orsay Cedex, France

P. Azzurri, G. Bagliesi, S. Bettarini, C. Bozzi, G. Calderini, V. Ciulli, R. Dell'Orso, R. Fantechi, I. Ferrante, A. Giassi, A. Gregorio, F. Ligabue, A. Lusiani, P.S. Marrocchesi, A. Messineo, F. Palla, G. Sanguinetti, A. Sciabà, G. Sguazzoni, J. Steinberger, R. Tenchini, C. Vannini, A. Venturi, P.G. Verdini

Dipartimento di Fisica dell'Università, INFN Sezione di Pisa, e Scuola Normale Superiore, 56010 Pisa, Italy

G.A. Blair, L.M. Bryant, J.T. Chambers, Y. Gao, M.G. Green, T. Medcalf, P. Perrodo, J.A. Strong, J.H. von Wimmersperg-Toeller

Department of Physics, Royal Holloway & Bedford New College, University of London, Surrey TW20 OEX, United Kingdom[10]

D.R. Botterill, R.W. Clifft, T.R. Edgecock, S. Haywood, P. Maley, P.R. Norton, J.C. Thompson, A.E. Wright

Particle Physics Dept., Rutherford Appleton Laboratory, Chilton, Didcot, Oxon OX11 OQX, United Kingdom[10]

B. Bloch-Devaux, P. Colas, B. Fabbro, W. Kozanecki, E. Lançon, M.C. Lemaire, E. Locci, P. Perez, J. Rander, J.-F. Renardy, A. Rosowsky, A. Roussarie, J.-P. Schuller, J. Schwindling, A. Trabelsi, B. Vallage

CEA, DAPNIA/Service de Physique des Particules, CE-Saclay, 91191 Gif-sur-Yvette Cedex, France[17]

S.N. Black, J.H. Dann, H.Y. Kim, A.M. Litke, M.A. McNeil, G. Taylor

Institute for Particle Physics, University of California at Santa Cruz, Santa Cruz, CA 95064, USA[19]

C.N. Booth, R. Boswell, C.A.J. Brew, S. Cartwright, F. Combley, M.S. Kelly, M. Lehto, W.M. Newton, J. Reeve, L.F. Thompson

Department of Physics, University of Sheffield, Sheffield S3 7RH, United Kingdom[10]

K. Affholderbach, A. Böhrer, S. Brandt, G. Cowan, J. Foss, C. Grupen, G. Lutters, P. Saraiva, L. Smolik, F. Stephan

Fachbereich Physik, Universität Siegen, 57068 Siegen, Fed. Rep. of Germany[16]

M. Apollonio, L. Bosisio, R. Della Marina, G. Giannini, B. Gobbo, G. Musolino

Dipartimento di Fisica, Università di Trieste e INFN Sezione di Trieste, 34127 Trieste, Italy

J. Putz, J. Rothberg, S. Wasserbaech, R.W. Williams

Experimental Elementary Particle Physics, University of Washington, WA 98195 Seattle, U.S.A.

S.R. Armstrong, E. Charles, P. Elmer, D.P.S. Ferguson, S. González, T.C. Greening, O.J. Hayes, H. Hu, S. Jin, P.A. McNamara III, J.M. Nachtman, J. Nielsen, W. Orejudos, Y.B. Pan, Y. Saadi, I.J. Scott, J. Walsh, Sau Lan Wu, X. Wu, J.M. Yamartino, G. Zobernig

Department of Physics, University of Wisconsin, Madison, WI 53706, USA[11]

[1]Now at Princeton University, Princeton, NJ 08544, U.S.A.

[2]Permanent address: Kangnung National University, Kangnung, Korea.

[3]Also at Dipartimento di Fisica, INFN Sezione di Catania, Catania, Italy.

[4]Also Istituto di Fisica Generale, Università di Torino, Torino, Italy.

[5]Also Istituto di Cosmo-Geofisica del C.N.R., Torino, Italy.

[6]Supported by the Commission of the European Communities, contract ERBCHBICT941234.

[7]Supported by CICYT, Spain.

[8]Supported by the National Science Foundation of China.

[9]Supported by the Danish Natural Science Research Council.

[10]Supported by the UK Particle Physics and Astronomy Research Council.

[11]Supported by the US Department of Energy, grant DE-FG0295-ER40896.

[12]Also at CERN, 1211 Geneva 23,Switzerland.

[13]Supported by the US Department of Energy, contract DE-FG05-92ER40742.

[14]Supported by the US Department of Energy, contract DE-FC05-85ER250000.

[15]Permanent address: Universitat de Barcelona, 08208 Barcelona, Spain.

[16]Supported by the Bundesministerium für Bildung, Wissenschaft, Forschung und Technologie, Fed. Rep. of Germany.

[17]Supported by the Direction des Sciences de la Matière, C.E.A.

[18]Supported by Fonds zur Förderung der wissenschaftlichen Forschung, Austria.

[19]Supported by the US Department of Energy, grant DE-FG03-92ER40689.

[20]Now at School of Operations Research and Industrial Engireering, Cornell University, Ithaca, NY 14853-3801, U.S.A.

[21]Now at Schweizerischer Bankverein, Basel, Switzerland.

1 Introduction

In the Minimal Supersymmetric Extension of the Standard Model (MSSM) [1] each Standard Model fermion has two scalar supersymmetric partners, one for each chirality state. The scalartops (stops) $\tilde{\mathrm{t}}_\mathrm{R}$ and $\tilde{\mathrm{t}}_\mathrm{L}$ are the supersymmetric partners of the top quark. These two fields are weak interaction eigenstates which mix to form the mass eigenstates. The stop mass matrix is given by [2]:

$$\begin{pmatrix} m^2_{\tilde{\mathrm{t}}_\mathrm{L}} & m_\mathrm{t} a_\mathrm{t} \\ m_\mathrm{t} a_\mathrm{t} & m^2_{\tilde{\mathrm{t}}_\mathrm{R}} \end{pmatrix},$$

where $m_{\tilde{\mathrm{t}}_\mathrm{R}}$ and $m_{\tilde{\mathrm{t}}_\mathrm{L}}$ are the $\tilde{\mathrm{t}}_\mathrm{R}$ and $\tilde{\mathrm{t}}_\mathrm{L}$ mass terms, a_t is related to the soft SUSY-breaking parameter A_t by $a_t = A_t - \mu/\tan\beta$ (where μ is the supersymmetric mass term which mixes the two Higgs superfields and $\tan\beta$ is the ratio between their vacuum expectation values) and m_t is the top quark mass. Since the off-diagonal terms of this matrix are proportional to m_t, the mixing between the weak interaction eigenstates may be large and the lighter stop could be the lightest supersymmetric charged particle. The stop mass eigenstates are obtained by a unitary transformation of the $\tilde{\mathrm{t}}_\mathrm{R}$ and $\tilde{\mathrm{t}}_\mathrm{L}$ fields, parametrised by the mixing angle $\theta_{\tilde{\mathrm{t}}}$. The lighter stop is given by $\tilde{\mathrm{t}} = \tilde{\mathrm{t}}_\mathrm{L}\cos\theta_{\tilde{\mathrm{t}}} + \tilde{\mathrm{t}}_\mathrm{R}\sin\theta_{\tilde{\mathrm{t}}}$, while the heavier stop is the orthogonal combination.

The stop could be produced at LEP in pairs, $\mathrm{e^+e^-} \to \tilde{\mathrm{t}}\bar{\tilde{\mathrm{t}}}$, via s-channel exchange of a virtual photon or a Z. The production cross section [3] depends on the stop charge for the coupling to the photon and on the weak mixing angle θ_W and the mixing angle $\theta_{\tilde{\mathrm{t}}}$ for the coupling to the Z. When $\theta_{\tilde{\mathrm{t}}}$ is about 56° the lightest stop decouples from the Z and its cross section is almost minimal. At $\sqrt{s} = 172$ GeV, the maximum cross section is of order 1 pb for a $\tilde{\mathrm{t}}$ mass of 60 GeV/c^2 and is reached for $\theta_{\tilde{\mathrm{t}}} = 0°$.

The searches for stops described here assume that all supersymmetric particles except the lightest neutralino χ and (possibly) the sneutrino $\tilde{\nu}$ are heavier than the stop. The conservation of R-parity is also assumed; this implies that the Lightest Supersymmetric Particle (LSP) is stable. Under these assumptions, the two dominant decay channels are $\tilde{\mathrm{t}} \to \mathrm{c}\chi$ or $\tilde{\mathrm{t}} \to \mathrm{b}\ell\tilde{\nu}$ [2]. The corresponding diagrams are shown in Figures 1a and 1b. The first decay can only proceed via loops and thus has a very small width, of the order of 1–0.01 eV [2].

The $\tilde{\mathrm{t}} \to \mathrm{b}\ell\tilde{\nu}$ channel proceeds via a virtual chargino exchange and has a width of the order of 0.1–10 keV [2], where the largest width is reached for a chargino mass close to the stop mass. This decay dominates when it is kinematically allowed. Assuming equal mass sneutrinos $\tilde{\nu}_\mathrm{e}$, $\tilde{\nu}_\mu$ and $\tilde{\nu}_\tau$, the lepton flavour for this decay is determined by the chargino composition. If the chargino is the supersymmetric partner of the W the decays $\tilde{\mathrm{t}} \to \mathrm{be}\tilde{\nu}_\mathrm{e}$, $\tilde{\mathrm{t}} \to \mathrm{b}\mu\tilde{\nu}_\mu$ and $\tilde{\mathrm{t}} \to \mathrm{b}\tau\tilde{\nu}_\tau$ occur with equal branching fractions. If the chargino is the supersymmetric partner of the charged Higgs the branching fraction of the decay $\tilde{\mathrm{t}} \to \mathrm{b}\tau\tilde{\nu}_\tau$ is enhanced. In all of these cases, if the neutralino is the LSP the sneutrino can decay into $(\chi\nu)$ but this invisible decay does not change the experimental topology.

A possible third stop decay channel is the four-body decay $\tilde{\mathrm{t}} \to \mathrm{b}f_1\bar{f}_2\chi$. One such four-body decay of the $\tilde{\mathrm{t}}$ is shown in Figure 1c. The rates of four-body decays are expected to be much smaller than that of the decay $\tilde{\mathrm{t}} \to \mathrm{c}\chi$.

The phenomenology of the scalar bottom (sbottom), the supersymmetric partner of the bottom quark, is similar to the phenomenology of the stop. In contrast to stops, sbottom mixing

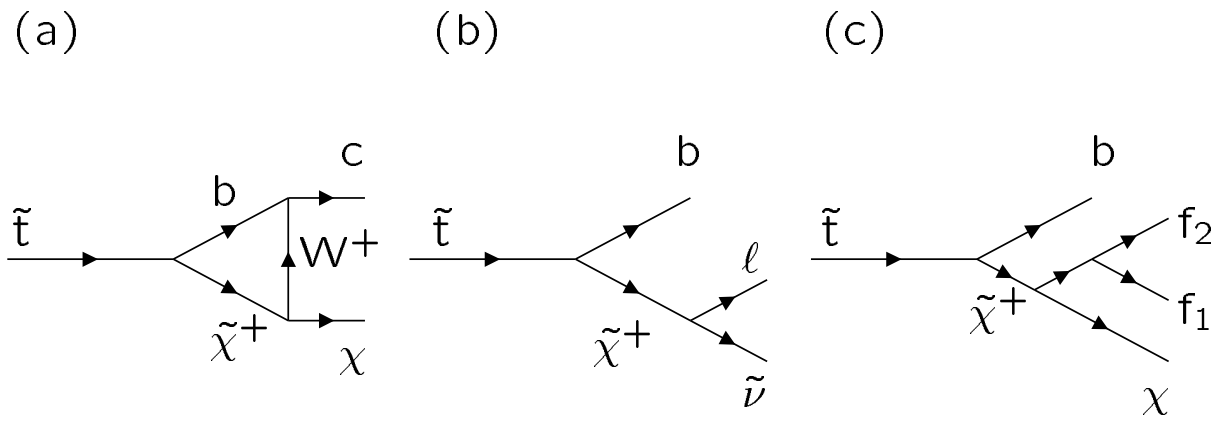

Figure 1: Stop decay diagrams. (a) $\tilde{\mathrm{t}} \to \mathrm{c}\chi$. (b) $\tilde{\mathrm{t}} \to \mathrm{b}\ell\tilde{\nu}$. (c) $\tilde{\mathrm{t}} \to \mathrm{b}\mathrm{f}_1\mathrm{f}_2\chi$. Decay (c) is not considered in this paper.

is expected to be large for large values of $\tan\beta$, because of the relation $a_b = A_b - \mu\tan\beta$. When the sbottom mixing angle $\theta_{\tilde{\mathrm{b}}}$ is about 68° the lightest sbottom decouples from the Z. Assuming that the $\tilde{\mathrm{b}}$ is lighter than all supersymmetric particles except the χ, the $\tilde{\mathrm{b}}$ will decay as $\tilde{\mathrm{b}} \to \mathrm{b}\chi$. Compared to the $\tilde{\mathrm{t}}$ decays, the $\tilde{\mathrm{b}}$ decay has a large width of the order of 10–100 MeV.

Direct searches for stops and sbottoms are performed for the stop decay channels $\tilde{\mathrm{t}} \to \mathrm{c}\chi$ and $\tilde{\mathrm{t}} \to \mathrm{b}\ell\tilde{\nu}$ and for the sbottom decay channel $\tilde{\mathrm{b}} \to \mathrm{b}\chi$. The results of these searches supersede the ALEPH results reported earlier for data collected at energies up to $\sqrt{s} = 136$ GeV [4]. The D0 experiment [5] has reported a lower limit on the stop mass of 85 GeV/c^2 for the decay into $\mathrm{c}\chi$ and for a mass difference between the $\tilde{\mathrm{t}}$ and the χ larger than about 40 GeV/c^2. Searches for $\tilde{\mathrm{t}} \to \mathrm{c}\chi$, $\tilde{\mathrm{t}} \to \mathrm{b}\ell\tilde{\nu}$ and $\tilde{\mathrm{b}} \to \mathrm{b}\chi$ using data collected at LEP at energies up to $\sqrt{s} = 172$ GeV have been performed by OPAL [6].

2 The ALEPH detector

A detailed description of the ALEPH detector can be found in Ref. [7], and an account of its performance as well as a description of the standard analysis algorithms can be found in Ref. [8]. Only a brief overview is given here.

Charged particles are detected in a magnetic spectrometer consisting of a silicon vertex detector (VDET), a drift chamber (ITC) and a time projection chamber (TPC), all immersed in a 1.5 T axial magnetic field provided by a superconducting solenoidal coil. Between the TPC and the coil, a highly granular electromagnetic calorimeter (ECAL) is used to identify electrons and photons and to measure their energy. Surrounding the ECAL is the return yoke for the magnet, which is instrumented with streamer tubes to form the hadron calorimeter (HCAL). Two layers of external streamer tubes are used together with the HCAL to identify muons.

The region near the beam line is covered by two luminosity calorimeters, the SICAL and the LCAL. The SICAL provides coverage from 34 to 63 mrad from the beamline while the LCAL provides coverage out to 160 mrad. The low angle coverage is completed by the HCAL, which occupies a position behind the LCAL and extends down to 106 mrad. The LCAL consists of two halves which fit together around the beamline; the area where the two halves come together

is a region of reduced sensitivity. This "vertical crack" accounts for only 0.05% of the total solid angle coverage of the ALEPH detector.

The information obtained from the tracking system is combined with the information obtained from the calorimeters to form a list of "energy flow particles" [8]. These objects are used to calculate the variables that are used in the analyses described in Section 4.

3 Monte Carlo Simulation

In the simulation of a stop signal, the most significant issues to be addressed are the treatment of the stop perturbative gluon radiation, hadronisation and decay.

Since the stop is a scalar particle, the spectrum of gluon emission differs from that of a quark. The standard shower evolution programs would therefore need modifications to include the gluon emission from a spin-zero particle. However, as pointed out in Ref. [9], the difference between the average energy loss due to perturbative gluon emission off a spin-0 and a spin-1/2 particle is small ($\lesssim 10^{-3}$) and can safely be neglected within the approximations used by most shower Monte Carlo codes.

The stop lifetime is longer than the typical hadronisation time of $O(10^{-23}$ s), which corresponds to a width of $O(0.1$ GeV). Stops therefore hadronise into colourless $(\tilde{\mathrm{t}}\bar{q})$ or $(\tilde{\mathrm{t}}qq)$ bound states before decaying. This is incorporated in the generator by letting stops hadronise as if they were ordinary quarks according to the LUND string fragmentation scheme implemented in JETSET 7.4 [10]. A Peterson fragmentation function [11] is used to describe the stop fragmentation. The $\epsilon_{\tilde{\mathrm{t}}}$ parameter in the function is scaled from b quarks following the relation $\epsilon_{\tilde{\mathrm{t}}} = \epsilon_{\mathrm{b}} m_{\mathrm{b}}^2/m_{\tilde{\mathrm{t}}}^2$ [11], with $\epsilon_{\mathrm{b}} = 0.0035$ [12] and $m_{\mathrm{b}} = 5$ GeV/c^2. Stop hadrons then decay according to a spectator model. The effective spectator quark mass M_{eff}, which takes into account non-perturbative effects, is set to 0.5 GeV/c^2. The decay quark, c or b depending on the decay channel, is allowed to develop a parton shower to take into account hard gluon emission. At the end of the parton shower, a string is stretched among all coloured particles.

A similar procedure is followed for the sbottom generator, taking into account the fact that the $\tilde{\mathrm{b}}$ lifetime is much shorter than the $\tilde{\mathrm{t}}$ lifetime. Depending on the $\tilde{\mathrm{b}}$ and χ mass difference and coupling, the $\tilde{\mathrm{b}}$ can decay either before or after hadronisation. Two sets of $\tilde{\mathrm{b}}$ signal samples, one for each of these possibilities, were generated over the same range of mass differences.

Signal samples were generated at $\sqrt{s} = 130$, 136, 161, and 172 GeV for various $(m_{\tilde{\mathrm{t}}}, m_\chi)$, $(m_{\tilde{\mathrm{b}}}, m_\chi)$ or $(m_{\tilde{\mathrm{t}}}, m_{\tilde{\nu}})$ masses. In these generations the mixing angle $\theta_{\tilde{\mathrm{t}}}$ or $\theta_{\tilde{\mathrm{b}}}$ was set to zero; the selection efficiency depends on the value of the mixing angle, since changing its value changes the spectrum of initial state radiation. Two sets of $\tilde{\mathrm{t}} \to \mathrm{b}\ell\tilde{\nu}$ samples have been produced. The first set assumes equal branching fractions for the $\tilde{\mathrm{t}}$ decay to e, μ or τ, while the second set assumes a branching fraction of 100% for the decay to τ. All of these samples were processed though the full ALEPH detector simulation.

The dependence of the selection efficiencies on the fragmentation parameters and on the mixing angle is discussed in Section 5. The effect of the short $\tilde{\mathrm{b}}$ lifetime on the $\tilde{\mathrm{b}}$ selection efficiency is also discussed in Section 5.

Monte Carlo samples corresponding to integrated luminosities at least 100 times that of

the data have been fully simulated for the annihilation processes $e^+e^- \to f\bar{f}$ and the various processes leading to four-fermion final states ($e^+e^- \to$ WW, $e^+e^- \to$ Weν, $e^+e^- \to$ Zee and $e^+e^- \to Z\gamma^*$). The two-photon processes $\gamma\gamma \to \ell^+\ell^-$ were simulated with an integrated luminosity about 20 times that of the data, while the two-photon processes $\gamma\gamma \to q\bar{q}$ were simulated with an integrated luminosity about three times that of the data.

4 Analysis

Data collected at $\sqrt{s}$ = 130, 136, 161, 170, and 172 GeV have been analysed, corresponding to integrated luminosities of 2.9, 2.9, 11.1, 1.1, and 9.5 pb^{-1}, respectively. To account for the dependence on $\sqrt{s}$, all cuts are performed in terms of variables normalised to the beam energy.

Two analyses are used to search for $\tilde{t}$ production. The first one is sensitive to the decay $\tilde{t} \to c\chi$ while the second one is sensitive to the decay $\tilde{t} \to b\ell\tilde{\nu}$. Both channels are characterised by missing momentum and energy. The experimental topology depends largely on Δm, the mass difference between the $\tilde{t}$ and the χ or $\tilde{\nu}$. When Δm is large, there is a substantial amount of energy available for the visible system and the signal events tend to look like WW, Weν, $Z\gamma^*$, and $q\bar{q}(\gamma)$ events. These processes are characterised by high multiplicity and high visible mass $M_{\rm vis}$. When Δm is small, the energy available for the visible system is small and the signal events are therefore similar to $\gamma\gamma \to q\bar{q}$ events. The process $\gamma\gamma \to q\bar{q}$ is characterised by low multiplicity, low $M_{\rm vis}$, low total transverse momentum $p_{\rm t}$ and the presence of energy near the beam axis. In order to cope with the different signal topologies and background situations, each analysis employs a low Δm selection and a high Δm selection.

The values of the analysis cuts are set in an unbiased way following the $\bar{N}_{95}$ procedure [13]. In this procedure, the cut values are varied and applied to the background samples and the signal samples in order to calculate $\bar{\sigma}_{95}$, the expected 95% Confidence Level (C.L.) limit on the signal cross section. The final cut values used in the analyses are the ones which minimise $\bar{\sigma}_{95}$. Cuts used to eliminate background from $\gamma\gamma \to q\bar{q}$ events are not varied. Such events are difficult to simulate when they go into the low angle region of the detector. Conservatively, the values of the cuts used against $\gamma\gamma \to q\bar{q}$ events are tighter than the values given by the $\bar{N}_{95}$ procedure.

The experimental topology of the process $e^+e^- \to \tilde{b}\bar{\tilde{b}}$ ($\tilde{b} \to b\chi$) is quite similar to that of the process $e^+e^- \to \tilde{t}\bar{\tilde{t}}$ ($\tilde{t} \to c\chi$). A common selection is therefore used to search for these two processes.

4.1 Search for $\tilde{t} \to c\chi$ and $\tilde{b} \to b\chi$

The processes $e^+e^- \to \tilde{t}\bar{\tilde{t}}$ ($\tilde{t} \to c\chi$) and $e^+e^- \to \tilde{b}\bar{\tilde{b}}$ ($\tilde{b} \to b\chi$) are characterised by two acoplanar jets and missing mass and energy. Two selections are employed, one for the small Δm case ($\Delta m < 10$ GeV/c^2) and one for the large Δm case ($\Delta m \geq 10$ GeV/c^2). A common preselection is used against $\gamma\gamma \to q\bar{q}$ events in both the low and high Δm analyses. The number of charged particle tracks $N_{\rm ch}$ must be at least four, $M_{\rm vis}$ must be larger than 4 GeV/c^2 and $p_{\rm t}$ (Figure 2a) must be larger than $2\%\sqrt{s}$, or $4\%\sqrt{s}$ if the missing momentum points to within 15° in azimuth

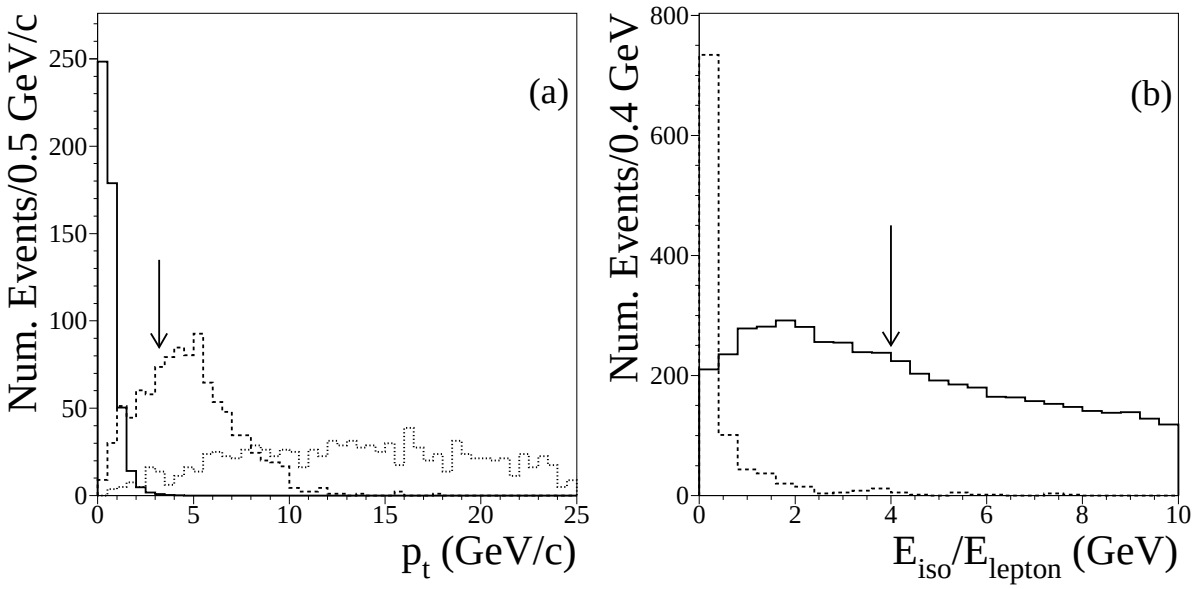

Figure 2: (a) p_t for $\gamma\gamma \to q\bar{q}$ and $\tilde{t} \to c\chi$ at $\sqrt{s} = 161$ GeV. The solid histogram gives the $\gamma\gamma \to q\bar{q}$ distribution, the dashed histogram gives the signal distribution for $m_{\tilde{t}} = 65$ GeV/c^2 and $\Delta m = 5$ GeV/c^2, the dotted histogram gives the signal distribution for $m_{\tilde{t}} = 65$ GeV/c^2 and $\Delta m = 15$ GeV/c^2. The cut $p_t > 2\%\sqrt{s}$ is indicated by the arrow. (b) E_{iso}/E_{lepton} for $q\bar{q}(\gamma)$ and $\tilde{t} \to b\ell\tilde{\nu}$ at $\sqrt{s} = 161$ GeV. The solid histogram gives the $q\bar{q}(\gamma)$ distribution, the dashed histogram gives the signal distribution for $m_{\tilde{t}} = 60$ GeV/c^2 and $\Delta m = 20$ GeV/c^2. The cut $E_{iso}/E_{lepton} < 4$ is indicated by the arrow. In (a), the cut $E_{12^\circ} = 0$ has been applied. In (b), at least one identified electron or muon is required. Normalization for the plots is arbitrary.

from the vertical crack in LCAL. The polar angle of the missing momentum vector, $\theta_{P_{miss}}$, must be greater than 18° and the energy detected within 12° of the beam axis, E_{12°, must be less than $5\%\sqrt{s}$. Both the acoplanarity and the transverse acoplanarity must be less than 175°. The acoplanarity is defined to be 180° for a back-to-back topology and is calculated from the momenta directions of the two event hemispheres, defined by a plane perpendicular to the thrust axis. The transverse acoplanarity is obtained by projecting the event onto a plane perpendicular to the beam axis, then calculating the two-dimensional thrust axis and dividing the event into two hemispheres by a plane perpendicular to that thrust axis. Both of these cuts are also effective against $q\bar{q}(\gamma)$ background.

4.1.1 Low Δm selection

Most of the cuts in the low Δm analysis are designed to eliminate the remaining background from $\gamma\gamma \to q\bar{q}$ events. The p_t cut is reinforced by calculating p_t excluding the neutral hadrons found by the energy flow algorithm and requiring it to be greater than $2\%\sqrt{s}$. The p_t is also calculated with only the charged particle tracks and required to be greater then $1\%\sqrt{s}$. These cuts eliminate $\gamma\gamma$ events that have a large p_t due to spurious calorimeter objects; these objects can occur when soft tracks are not correctly associated with deposits in the ECAL or HCAL.

Such events are also eliminated by asking that the most energetic neutral hadronic deposit be less than 30% of the total visible energy $E_{\rm vis}$. To eliminate $\gamma\gamma$ events that pass the $p_{\rm t}$ cuts, E_{12° must be equal to zero, $\theta_{P_{\rm miss}}$ must be greater than 37°, $\theta_{\rm thrust}$, the polar angle of the thrust axis, must be greater than 41°, and the missing mass $M_{\rm miss}$ divided by $M_{\rm vis}$ must be less than 25. Also of use is the fact that the missing momentum in $\gamma\gamma \to q\bar{q}$ and $q\bar{q}(\gamma)$ events can arise from neutrinos produced in semileptonic decays. When these decays occur within a jet, the resulting missing $p_{\rm t}$ is not isolated. Signal events are therefore selected by requiring the energy $E_{\rm w}$ in a 30° azimuthal wedge around the direction of missing $p_{\rm t}$ to be less than $25\%\sqrt{s}$.

If a scattered electron from a $\gamma\gamma \to q\bar{q}$ process goes into an insensitive region of the detector, only a small fraction of the electron energy may be recorded. The missing electron energy can lead to a large measured $p_{\rm t}$, faking a signal. These fake signals can be eliminated by calculating the scattered electron angle $\theta_{\rm scat}$ from the $p_{\rm t}$, assuming the other electron to be undeflected, and by computing the angle $\theta_{\rm point}$ between the calculated electron direction and the closest energy deposit. The fake signals surviving the $p_{\rm t}$ cut usually have a large value of $\theta_{\rm scat}$, because the $p_{\rm t}$ imbalance is large, and a small value of $\theta_{\rm point}$, because the calculated electron direction points to the energy deposit from the scattered electron. Both $\theta_{\rm scat}$ and $\theta_{\rm point}$ are incorporated into the analysis through the cut $\theta_{\rm point} > 60^\circ - 10 \times \theta_{\rm scat}$.

Additional cuts are used against the $\gamma\gamma \to \tau^+\tau^-$ background. Most of the $\gamma\gamma \to \tau^+\tau^-$ events that survive the above cuts have four charged particle tracks from the decays $\tau \to$ one-prong, $\tau \to$ three-prong, and the low visible mass and high value of acoplanarity characteristic of $\gamma\gamma$ events in general. In order to eliminate these events, any four-track event must have transverse acoplanarity less than 150° or visible mass greater than 20 GeV/c^2. As an additional safeguard, all four-track events are required to have a visible mass larger than 8 GeV/c^2 regardless of the value of the transverse acoplanarity.

The low Δm analysis is completed by applying cuts against low mass WW, Zγ^*, and Weν events. A cut of thrust < 0.97 is effective against Zγ^* (with Z $\to \nu\bar{\nu}$), while WW and Weν events are eliminated by requiring that $E_{\rm vis}$ be less than $26\%\sqrt{s}$. Events from the process WW $\to \ell\nu_\ell\tau\nu_\tau$, where the τ subsequently undergoes a three-prong decay, are eliminated by requiring that the event mass excluding identified electrons and muons be greater than 3 GeV/c^2.

4.1.2 High Δm selection

The main background in the high Δm case comes from WW, Weν, Zγ^*, and $q\bar{q}(\gamma)$. Events from $\gamma\gamma$ processes may still contribute to the background because they have a very large cross section and because detector effects may lead to extreme values for variables such as $p_{\rm t}$. Background from $\gamma\gamma$ is reduced by requiring that $N_{\rm ch}$ be greater than six and that $p_{\rm t}$ be greater than $5\%\sqrt{s}$, or $7.5\%\sqrt{s}$ if the missing momentum points to within 15° of the vertical LCAL crack. Additional $\gamma\gamma$ events are removed by requiring that $p_{\rm t}$ be greater than $20\%E_{\rm vis}$. As in the low Δm selection, it is necessary to guard against $\gamma\gamma$ events that have a large $p_{\rm t}$ due to a missed association between soft tracks and calorimetry deposits. This is done by demanding that the total energy from neutral hadrons be less than $30\%E_{\rm vis}$; this is relaxed to $45\%E_{\rm vis}$ if the $p_{\rm t}$ calculated without neutral hadrons is greater than $3\%\sqrt{s}$. Other cuts which are effective against $\gamma\gamma$ events are $\theta_{\rm point} > 5^\circ$, $E_{\rm w} < 7.5\%\sqrt{s}$ and the total energy more than 30° away from

the beam greater than $30\% E_{\rm vis}$.

Finally, cuts against WW, Weν, and Zγ^* are applied. Events from Zγ^* are eliminated by requiring that the thrust be less than 0.935. To eliminate WW events in which one of the W's decays leptonically, any identified electron or muon must have an energy less than $20\%\sqrt{s}$. In order to further reduce background from WW and Weν events, an upper cut is applied on the visible mass. The optimal value of this cut as determined by the $\bar{N}_{95}$ procedure depends on the mass difference of the signal sample considered. A hypothesis of $\Delta m = 15$ GeV/c^2 gives an optimal value of $0.315\sqrt{s}$ for the $M_{\rm vis}$ cut while a hypothesis of $\Delta m \geq 35$ GeV/c^2 gives an optimal value of $0.375\sqrt{s}$ for the $M_{\rm vis}$ cut.

The high Δm selection changes as a function of Δm through the $M_{\rm vis}$ cut. When this selection is applied to the data, the loosest $M_{\rm vis}$ cut is used. In the case that limits must be set, a candidate is counted for a given value of Δm only if it has a visible mass less than the $M_{\rm vis}$ cut used for that value of Δm.

4.1.3 Selection efficiency and background

To combine the low and high Δm selections, three possibilities are considered: the low Δm selection may be used, the high Δm selection may be used, or both selections may be used. According to the $\bar{N}_{95}$ procedure the two selections should not be used simultaneously for any value of Δm. For $\Delta m < 10$ GeV/c^2, the low Δm selection is used, while for $\Delta m \geq 10$ GeV/c^2, the high Δm selection is used. The $\tilde{\rm t}$ efficiencies are shown in Figure 3a while the $\tilde{\rm b}$ efficiencies are shown in Figure 3b. These $\tilde{\rm b}$ efficiencies are evaluated assuming that the $\tilde{\rm b}$ hadronises before it decays.

For the low Δm selection, the requirement that $E_{12^\circ} = 0$ results in an inefficiency due to beam-related and detector background. The size of this effect ($\sim 4\%$) has been measured using events triggered at random beam crossings and the low Δm selection efficiency is decreased accordingly.

The background to the low Δm selection is dominated by $\gamma\gamma \to q\bar{q}$ and $\gamma\gamma \to \tau^+\tau^-$ and has a total expectation of 0.9 events (~ 40 fb) at $\sqrt{s} = 161$–172 GeV and 0.2 events (~ 30 fb) at $\sqrt{s} = 130$–136 GeV. For the high Δm selection, the background is dominated by WW, Weν, Zγ^*, and $q\bar{q}(\gamma)$ at $\sqrt{s} = 161$–172 GeV and by $q\bar{q}(\gamma)$ at $\sqrt{s} = 130$–136 GeV. The total background expectation for this selection is 1.0 event (~ 50 fb) at $\sqrt{s} = 161$–172 GeV and 0.2 events (~ 30 fb) at $\sqrt{s} = 130$–136 GeV, using the loosest value of the $M_{\rm vis}$ cut.

4.2 Search for $\tilde{\rm t} \to {\rm b}\ell\tilde{\nu}$

The experimental signature for $\tilde{\rm t} \to {\rm b}\ell\tilde{\nu}$ is two acoplanar jets plus two leptons with missing momentum. The leptons tend to have low momenta, especially for low Δm signals; when Δm is 8 GeV/c^2, the most energetic lepton often has a momentum between 1 and 2 GeV/c. In order to identify electrons and muons, loose identification criteria based on the pattern of deposits in the ECAL and the HCAL have been applied. These loose criteria allow 1 GeV/c electrons and 1.5 GeV/c muons to be identified. Since low-momenta lepton candidates are often misidentified pions, other analysis cuts must be used to keep the background at a low level. Two

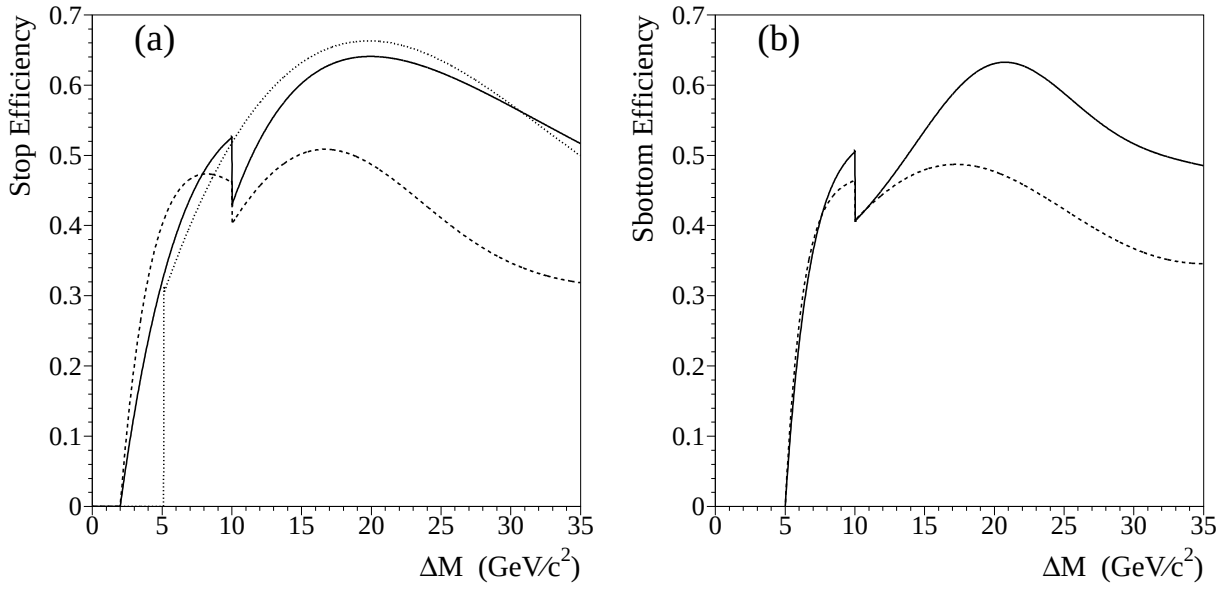

Figure 3: Efficiencies as a function of Δm. (a) Efficiency for a 65 GeV/c^2 stop decaying as $\tilde{\mathrm{t}} \to \mathrm{c}\chi$ (solid curve), a 50 GeV/c^2 stop decaying as $\tilde{\mathrm{t}} \to \mathrm{c}\chi$ (dashed curve) and a 60 GeV/c^2 stop decaying as $\tilde{\mathrm{t}} \to \mathrm{b}\ell\tilde{\nu}$ (dotted curve). (b) Efficiency for a 60 GeV/c^2 sbottom (solid curve) and a 50 GeV/c^2 sbottom (dashed curve) decaying as $\tilde{\mathrm{b}} \to \mathrm{b}\chi$.

selections are used, one for the small Δm case ($\Delta m < 10$ GeV/c^2) and the other for the large Δm case ($\Delta m \geq 10$ GeV/c^2). A preselection common to both the low and high Δm selections is used against the $\gamma\gamma \to q\bar{q}$ background. It is required that N_{ch} be greater than six and M_{vis} be greater than $8\%\sqrt{s}$. It is also required that p_{t} be greater than $1.25\%\sqrt{s}$, E_{12° be smaller than 2 GeV, and θ_{point} be greater than $50^\circ - 20 \times \theta_{\mathrm{scat}}$. In order to eliminate the radiative $f\bar{f}\gamma$ events in which a return to the Z peak has occurred, events with a longitudinal momentum greater than $30\%\sqrt{s}$ are rejected.

4.2.1 Low Δm selection

If Δm is small the visible energy is also small and both the jets and leptons are very soft. Since very soft leptons might not be identified, events with no electrons or muons are accepted. The main background arises from $\gamma\gamma \to q\bar{q}$. It is therefore required that $E_{12^\circ} = 0$ and that both $\theta_{P_{\mathrm{miss}}}$ and θ_{thrust} be greater than 37°. An acoplanarity between 100° and 179° is also required. There must be at least one electron or muon with momentum greater than $1\%\sqrt{s}$, otherwise both the p_{t} cut and the two-dimensional cut in the θ_{point}-θ_{scat} plane are tightened: $p_{\mathrm{t}} > 2\%\sqrt{s}$, $\theta_{\mathrm{point}} > 115^\circ - 20 \times \theta_{\mathrm{scat}}$.

The WW background is eliminated by requiring that the missing mass be greater than $82.5\%\sqrt{s}$ and that the hadronic mass be smaller than $5\%\sqrt{s}$ if at least one electron or muon is identified. The $q\bar{q}(\gamma)$ events are rejected by requiring that the thrust be smaller than 0.9.

4.2.2 High Δm selection

For large mass differences at least one electron or muon with momentum between 2 and 35 GeV/c is required. It is further required that $E_{\rm iso}$, the energy in a 30° cone around the direction of the electron or muon momentum (Figure 2b), be smaller than four times the electron or muon energy. If a second electron or muon is identified, $E_{\rm iso}$ is required to be smaller than 10 times the electron or muon energy. If only one electron or muon is found, a tau jet is selected using the JADE algorithm with $y_{\rm cut} = 0.001$. This candidate τ jet must have an energy smaller than 30 GeV, have less than 2 GeV of energy carried by neutral hadrons, and have an angle of at least 20° with the nearest jet. Finally, the missing mass is required to be greater than $25\%\sqrt{s}$.

To reinforce the $\gamma\gamma \to q\bar{q}$ rejection further cuts are needed. It is required that $\theta_{P_{\rm miss}}$ be greater than 18°, that the transverse acoplanarity be smaller than 176° and that the acollinearity be smaller than 174°. If only one electron or muon is identified the hadronic neutral mass must be smaller than $30\%E_{\rm vis}$ and the cuts on $\theta_{P_{\rm miss}}$ and $p_{\rm t}$ are tightened: $\theta_{P_{\rm miss}} > 26°$, $p_{\rm t} > 3\%\sqrt{s}$

The WW background events are eliminated by requiring that $M_{\rm vis}$ be smaller than $74\%\sqrt{s}$ and that the hadronic mass be less than $37\%\sqrt{s}$. It is also required that the quadratic mean of the two inverse hemisphere boosts ($\sqrt{((m_1/E_1)^2 + (m_2/E_2)^2)/2}$ with $m_{1,2}$ and $E_{1,2}$ the two hemisphere masses and energies) be greater than 0.2. The remaining $q\bar{q}(\gamma)$ background is reduced by requiring that the thrust be smaller than 0.925.

4.2.3 Selection efficiency and background

The low and high Δm selections are combined using the same procedure as in Section 4.1.3. In contrast to the situation for the $\tilde{\rm t} \to {\rm c}\chi$ channel, the smallest value of $\bar{\sigma}_{95}$ is obtained when the low and high Δm selections are used simultaneously. This is true for all values of Δm. Shown in Figure 3a is the efficiency assuming equal branching fractions for the $\tilde{\rm t}$ decay to e, μ or τ. If the branching ratio to τ is 100%, the efficiency is about 35% for a Δm between 10 and 35 GeV/c^2. As is the case for the $\tilde{\rm t} \to {\rm c}\chi$ channel, the inefficiency caused by the beam-related and detector background is taken into account.

Most of the background comes from the high Δm selection and is dominated by $q\bar{q}(\gamma)$ at $\sqrt{s}$ = 130–161 GeV and by WW and $q\bar{q}(\gamma)$ at $\sqrt{s}$ = 170–172 GeV. A total of 0.8 events ($\sim$ 30 fb at 161 GeV and $\sim$ 50 fb at 172 GeV) are expected at $\sqrt{s}$ = 161–172 GeV while 0.2 events ($\sim$ 30 fb) are expected at $\sqrt{s}$ = 130–136 GeV.

5 Systematic Uncertainties

The systematic uncertainty on the $\tilde{\rm t}$ and $\tilde{\rm b}$ selection efficiencies comes mainly from the limited knowledge of $\tilde{\rm t}$ and $\tilde{\rm b}$ physics (hadronisation and decay). Uncertainties related to detector effects, to the size of the signal samples, and to the parameterisation of the signal efficiencies are also considered, and for the $\tilde{\rm t} \to {\rm b}\ell\tilde{\nu}$ analysis the effects of lepton identification are taken into account. The physics model used in the generators is described in Section 3; the systematic

effects are studied by varying the parameters of the model and checking the resultant effect on the efficiency.

The change in the efficiency due to the systematic effects is shown in Table 3. When Δm is small, the uncertainties associated with the $\tilde{\mathrm{t}}$ and $\tilde{\mathrm{b}}$ physics are relevant. The largest change in the low Δm efficiency comes from the variation in M_{eff}. This variation changes the invariant mass available for the hadronic system and thus the multiplicity and event shape. To quantify these effects, M_{eff} is varied from 0.3 GeV/c^2 to 1.0 GeV/c^2, a range much larger than that implied by low energy measurements. When Δm is large, the selection efficiencies are insensitive to the values of the parameters, changing by only $\sim 2\%$ relative even for $M_{\mathrm{eff}} = 2$ GeV/c^2.

The fragmentation parameters are varied over a range suggested by LEP1 measurements. In the case of $\epsilon_{\tilde{\mathrm{t}}}$ the error is propagated from ϵ_{b} according to the formula described in Section 3, and for the $\tilde{\mathrm{t}} \to \mathrm{b}\ell\tilde{\nu}$ channel ϵ_{b} is varied simultaneously with $\epsilon_{\tilde{\mathrm{t}}}$. Similarly, for the $\tilde{\mathrm{b}} \to \mathrm{b}\chi$ channel ϵ_{b} is varied simultaneously with $\epsilon_{\tilde{\mathrm{b}}}$. For the large Δm case the fragmentation parameters are varied more drastically, but even drastic variations have little effect on the efficiency; for instance, when $\epsilon_{\tilde{\mathrm{t}}} = \epsilon_{\mathrm{b}}$, the relative change in large Δm $\tilde{\mathrm{t}}$ efficiencies is only $\sim 2\%$.

The systematic effect of varying the mixing angles is quantified by evaluating the efficiencies on a set of $\tilde{\mathrm{t}}$ samples generated with $\theta_{\tilde{\mathrm{t}}} = 56^\circ$ and on a set of $\tilde{\mathrm{b}}$ samples generated with $\theta_{\tilde{\mathrm{b}}} = 68^\circ$. For these values of mixing, the stops and sbottoms decouple from the Z and the change in efficiencies due to differing amounts of initial state radiation is maximal.

The structure of the matrix element [2] in the semileptonic decay $\tilde{\mathrm{t}} \to \mathrm{b}\ell\tilde{\nu}$ is also considered. Two sets of $\tilde{\mathrm{t}} \to \mathrm{b}\ell\tilde{\nu}$ signal samples are generated. One set includes the the matrix element, treated as in Reference 2, while the other set employs a phase space decay model. Including the matrix element increases the efficiency of the $\tilde{\mathrm{t}} \to \mathrm{b}\ell\tilde{\nu}$ selection by about 5% relative with respect to the phase space decay model. Conservatively, the phase space decay model is used to obtain the $\tilde{\mathrm{t}} \to \mathrm{b}\ell\tilde{\nu}$ efficiencies.

The effect of the relatively short $\tilde{\mathrm{b}}$ lifetime has been checked by comparing the two sets of $\tilde{\mathrm{b}}$ signal samples. Higher efficiencies are always obtained from the set in which the $\tilde{\mathrm{b}}$ decays before hadronisation. The lower efficiencies, obtained under the assumption that the $\tilde{\mathrm{b}}$ hadronises before decay, are taken as the actual efficiencies; this helps ensure that any limits set on $\tilde{\mathrm{b}}$ production will be conservative.

The size of the signal samples, 1000 events, leads to a relative uncertainty of less than 2%, while the parameterisation of the signal efficiencies leads to an additional relative uncertainty of $\sim 2\%$. The total statistical uncertainty associated with the Monte Carlo signal simulation is therefore $\sim 3\%$ relative.

Detector effects have been studied for the variables used in the analyses. Events in the data from $q\bar{q}(\gamma)$ final states are selected with a loose set of cuts and compared with the $q\bar{q}(\gamma)$ Monte Carlo. All of the relevant variables, such as p_{t} and θ_{point}, show good agreement. The lepton isolation and the lepton identification, which are crucial for the $\tilde{\mathrm{t}} \to \mathrm{b}\ell\tilde{\nu}$ analysis, are also considered. The lepton isolation shows good agreement between $q\bar{q}(\gamma)$ Monte Carlo and data, while the lepton identification is found to lead to a 3% systematic error.

The systematic errors are incorporated into the final result using the method described in Reference [14].

Table 1: Summary of relative systematic uncertainties on the $\tilde{t}$ and $\tilde{b}$ selection efficiencies. The ranges of variation are those used for the low Δm case.

Systematic Uncertainties (%)						
Type	$\tilde{t} \to c\chi$		$\tilde{b} \to b\chi$		$\tilde{t} \to b\ell\tilde{\nu}$	
	High Δm	Low Δm	High	Low	High	Low
$M_{\rm eff}$ (0.3–1.0 GeV/c^2)	3	10	4	11	3	15
$\epsilon_{\tilde{t}}, \epsilon_b(\epsilon_b 0.002 - 0.006)$	2	2	-	-	2	2
$\epsilon_{\tilde{b}}, \epsilon_b(\epsilon_b 0.002 - 0.006)$	-	-	1	2	-	-
ϵ_c (0.02–0.06)	3	7	-	-	-	-
$\theta_{\tilde{t}}$ (0°–56°)	1	3	-	-	2	1
$\theta_{\tilde{b}}$ (0°–68°)	-	-	3	2	-	-
Monte Carlo statistics	3	3	3	3	3	3
detector effects	*negl.*	*negl.*	*negl.*	*negl.*	3	3
TOTAL	6	13	6	12	6	16

6 Results

One event is selected by the $\tilde{t} \to c\chi$, $\tilde{b} \to b\chi$ selection, while no events are selected by the $\tilde{t} \to b\ell\tilde{\nu}$ selection. The candidate event is selected at $\sqrt{s} = 161$ GeV; its kinematic properties suggest the process $e^+e^- \to Z\gamma^* \to \nu\bar{\nu}\tau^+\tau^-$ as a Standard Model interpretation. Since only a single event is selected, it is appropriate to set lower limits on the masses of the $\tilde{t}$ and $\tilde{b}$. Figures 4a, 4b, and 4c give the 95% C.L. excluded regions for the channel $\tilde{t} \to c\chi$. For this channel, the $\theta_{\tilde{t}}$-independent lower limit on $m_{\tilde{t}}$ is 67 GeV/c^2, assuming a mass difference between the $\tilde{t}$ and the χ of at least 10 GeV/c^2. Figures 5a, 5b, and 5c give excluded regions for the $\tilde{t} \to b\ell\tilde{\nu}$ channel, assuming equal branching ratios for the $\tilde{t}$ decay to e, μ, τ. In this case, the $\theta_{\tilde{t}}$-independent lower limit on $m_{\tilde{t}}$ is 70 GeV/c^2, assuming a mass difference between the $\tilde{t}$ and the $\tilde{\nu}$ of at least 10 GeV/c^2.

Figure 5d gives the excluded region in the $(\Delta m, m_{\tilde{t}})$ plane for the $\tilde{t} \to b\ell\tilde{\nu}$ channel, assuming a branching ratio of 100% for the $\tilde{t}$ decay to τ. A $\theta_{\tilde{t}}$-independent lower limit of 64 GeV/c^2 is set on $m_{\tilde{t}}$ in this case, again assuming a mass difference between the $\tilde{t}$ and the $\tilde{\nu}$ of at least 10 GeV/c^2.

Figures 6a, 6b and 6c give the excluded regions for the $\tilde{b}$ decay $\tilde{b} \to b\chi$. A lower limit of 73 GeV/c^2 is set on $m_{\tilde{b}}$, assuming that $\theta_{\tilde{b}}$ is 0° and that the mass difference between the $\tilde{b}$ and the χ is at least 10 GeV/c^2. Figure 6b shows that $\theta_{\tilde{b}}$-independent $m_{\tilde{b}}$ limits are not set. When decoupling from the Z occurs, sbottoms can only be produced through photon exchange and the cross section for the $\tilde{b}$ (charge $-1/3$) is four times lower than the cross section for the $\tilde{t}$ (charge $+2/3$).

7 Conclusions

Searches have been performed for scalar top quarks at $\sqrt{s} = 130$–172 GeV. A single candidate event, selected at $\sqrt{s} = 161$ GeV, is observed in the $\tilde{t} \to c\chi$ channel while no events are observed in the $\tilde{t} \to b\ell\tilde{\nu}$ channel. This is consistent with the background expectations of 2.3 events for the $\tilde{t} \to c\chi$ channel and 1.0 events for the $\tilde{t} \to b\ell\tilde{\nu}$ channel.

A 95 % C.L. limit of $m_{\tilde{t}} > 67$ GeV/c^2 is obtained for the $\tilde{t} \to c\chi$ channel, independent of the mixing angle and valid for a mass difference between the $\tilde{t}$ and the χ larger than 10 GeV/c^2. For the $\tilde{t} \to b\ell\tilde{\nu}$ channel, the $\theta_{\tilde{t}}$-independent limit is $m_{\tilde{t}} > 70$ GeV/c^2 if the mass difference between the $\tilde{t}$ and the $\tilde{\nu}$ is greater than 10 GeV/c^2 and if the branching ratios are equal for the $\tilde{t}$ decays to e, μ, and τ.

A limit is also obtained for the $\tilde{b}$ decaying as $\tilde{b} \to b\chi$. The limit is $m_{\tilde{b}} > 73$ GeV/c^2 for the supersymmetric partner of the left-handed state of the bottom quark if the mass difference between the $\tilde{b}$ and the χ is greater than 10 GeV/c^2.

8 Acknowledgements

We wish to congratulate our colleagues from the accelerator divisions for the successful operation of LEP above the W^+W^- threshold. We would also like to express our gratitude to the engineers and support people at our home institutes without whom this work would not have been possible. Those of us from non-member states wish to thank CERN for its hospitality and support.

References

[1] H.P. Nilles, Phys. Rep. **C 110** (1984) 1;
H.E. Haber and G.L. Kane, Phys. Rep. **C 117** (1985) 75;
R. Barbieri, Riv. Nuovo Cimento **11**, (1988) 1.

[2] K. Hikasa and M. Kobayashi, Phys. Rev. **D 36** (1987) 724.

[3] M. Drees and K. Hikasa, Phys. Lett. **B 252** (1990) 127.

[4] ALEPH Collaboration, Phys. Lett. **B 373** (1996) 246.

[5] D0 Collaboration, Phys. Rev. Letters **77** (1996) 2222.

[6] OPAL Collaboration, "*Search for Scalar Top and Scalar Bottom Quarks at $\sqrt{s}$ = 170 – 172 GeV in* e^+e^- *Collisions*", CERN-PPE 97-046. To be published in Z. Phys. **C**.

[7] ALEPH Collaboration, Nucl. Instrum. and Methods **A 294** (1990) 121.

[8] ALEPH Collaboration, Nucl. Instrum. and Methods **A 360** (1995) 481.

[9] W. Beenakker, R. Hopker, M. Spira and P.M. Zerwas, Phys. Lett. **B 349** (1995) 463. *Physics at LEP2*, CERN 96-01 (1996), Eds G. Altarelli, T. Sjöstrand and F. Zwirner, Vol. 2.

[10] T. Sjöstrand, Comput. Phys. Commun. **82** (1994) 74.

[11] C. Peterson, D. Schlatter, I. Schmitt and P.M. Zerwas, Phys. Rev. **D 27** (1983) 105.

[12] ALEPH Collaboration, "*Studies of Quantum Chromodynamics with the ALEPH Detector*", CERN-PPE 96-186. To be published in Physics Reports.

[13] The ALEPH Collaboration, Phys. Lett. **B 384** (1996) 427.

[14] R.D. Cousins and V.L. Highland, Nucl. Instrum. and Methods **A320** (1992) 331.

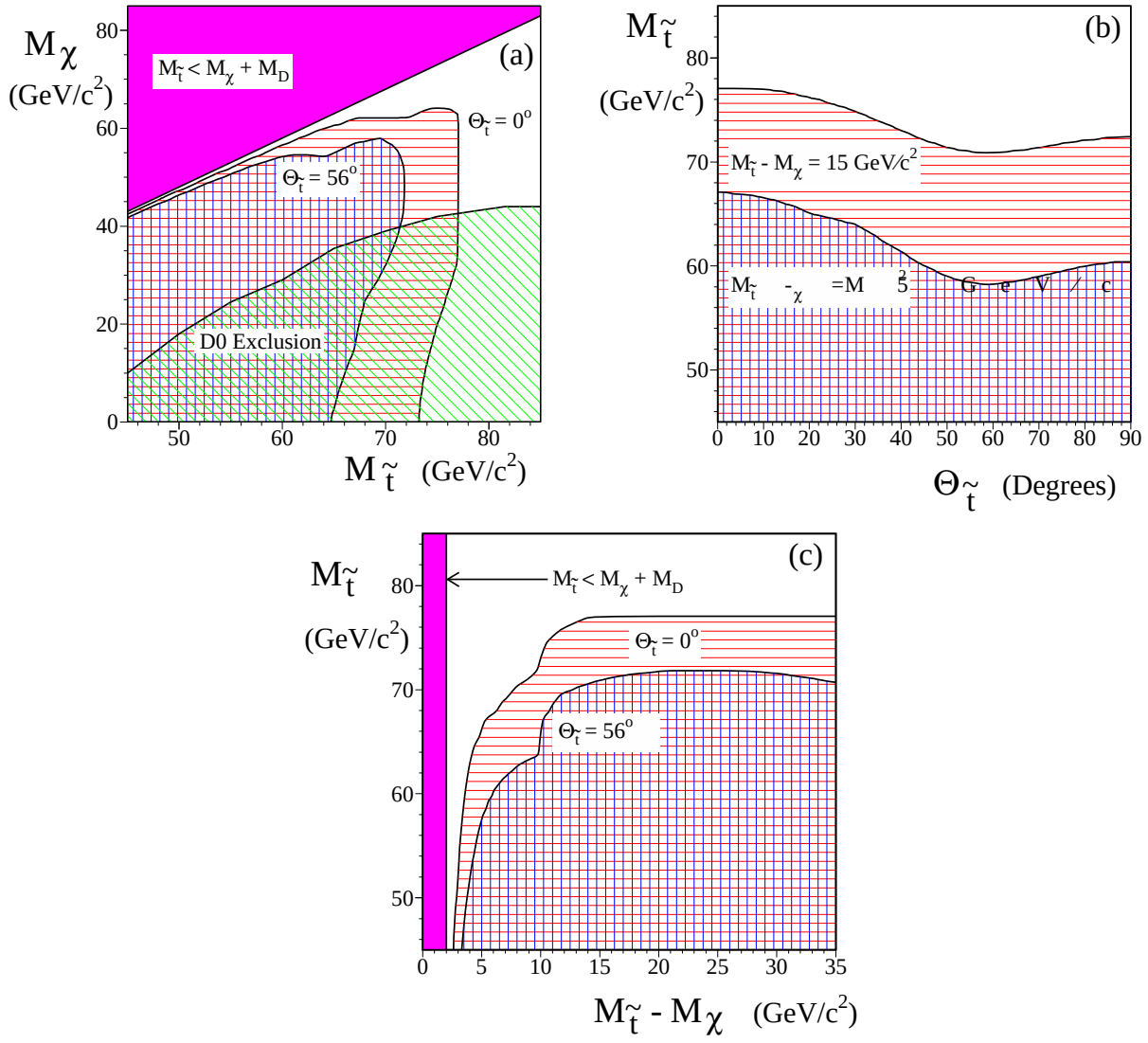

Figure 4: Excluded regions assuming $\tilde{t} \to c\chi$. (a) Excluded region in the m_χ vs $m_{\tilde{t}}$ plane, including the region excluded by the D0 collaboration. (b) Excluded region in the $m_{\tilde{t}}$ vs $\theta_{\tilde{t}}$ plane. (c) Excluded region in the $m_{\tilde{t}}$ vs Δm plane. In (a) and (c), excluded regions are given for 0°, corresponding to the maximum $\tilde{t}$-Z coupling, and for 56°, corresponding to the minimum $\tilde{t}$-Z coupling.

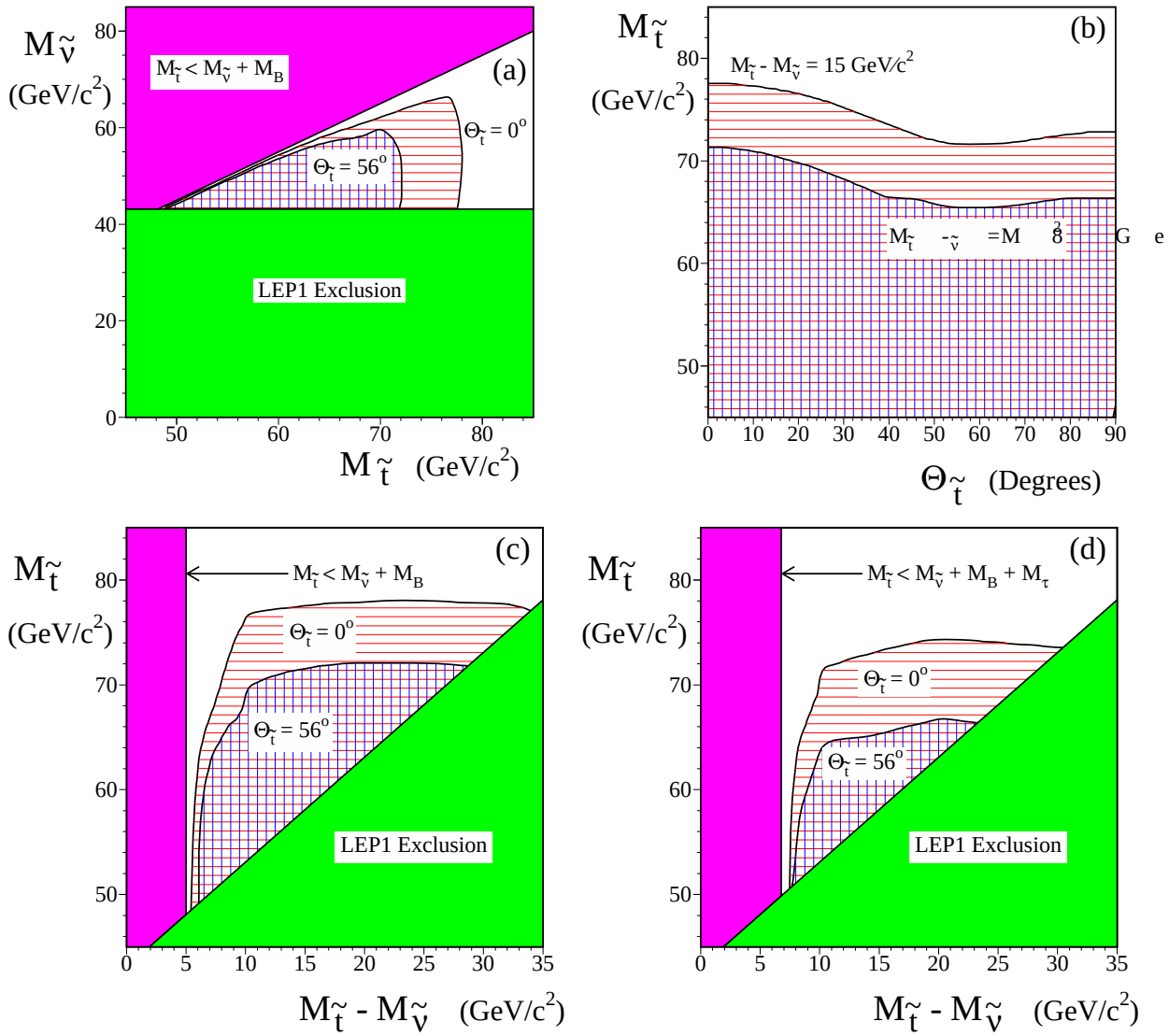

Figure 5: Excluded regions assuming $\tilde{t} \to b\ell\tilde{\nu}$. (a) Excluded region in the $m_{\tilde{\nu}}$ vs $m_{\tilde{t}}$ plane. (b) Excluded region in the $m_{\tilde{t}}$ vs $\theta_{\tilde{t}}$ plane. (c) Excluded region in the $m_{\tilde{t}}$ vs Δm plane. In (a), (b) and (c) equal branching fractions for the $\tilde{t}$ decay to e, μ or τ are assumed. (d) Excluded region in the $m_{\tilde{t}}$ vs Δm plane, assuming a branching ratio of 100% for the $\tilde{t}$ decay to τ. In (a), (c), and (d), excluded regions are given for 0°, corresponding to the maximum $\tilde{t}$-Z coupling, and for 56°, corresponding to the minimum $\tilde{t}$-Z coupling. Also shown in (a), (c), and (d) is the excluded region from LEP1, obtained from the measurement of the Z lineshape.

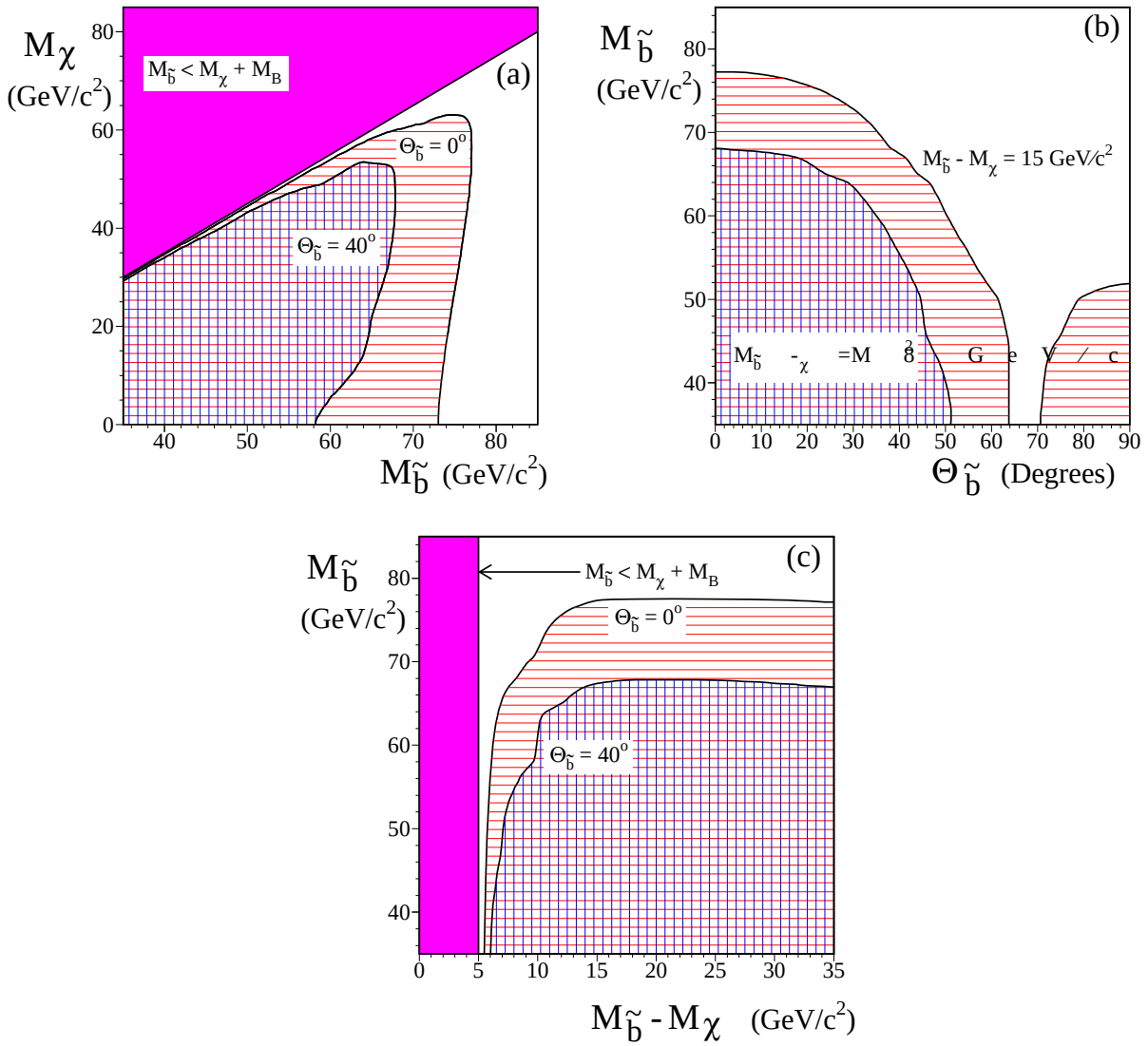

Figure 6: Excluded regions assuming $\tilde{b} \rightarrow b\chi$. (a) Excluded region in the m_{χ} vs $m_{\tilde{b}}$ plane. (b) Excluded region in the $m_{\tilde{b}}$ vs $\theta_{\tilde{b}}$ plane. (c) Excluded region in the $m_{\tilde{b}}$ vs Δm plane. In (a) and (c), excluded regions are given for 0°, corresponding to the maximum $\tilde{b}$-Z coupling, and for 40°.